KU LEUVEN

STADIUS
Center for Dynamical Systems, Signal Processing and Data Analytics

Citation/Reference	Laudadio T., Croitor Sava A.R., Sima D.M., Wright A.J., Heerschap A., Mastronardi N., Van Huffel S., ``Hierarchical non-negative matrix factorization applied to three-dimensional 3T MRSI data for automatic tissue charcterisation of the prostate'', *NMR in Biomedicine*, 2016, pp. 1-8
Archived version	Final publisher's version / pdf
Published version	insert link to the published version of your paper http://dx.doi.org/10.1002/nbm.3527
Journal homepage	http://www.wileyonlinelibrary.com
IR	url in Lirias https://lirias.kuleuven.be/handle/123456789/533781

(article begins on next page)

Research article

NMR IN BIOMEDICINE

Received: 18 February 2015, Revised: 1 March 2016, Accepted: 1 March 2016, Published online in Wiley Online Library

(wileyonlinelibrary.com) DOI: 10.1002/nbm.3527

Hierarchical non-negative matrix factorization applied to three-dimensional 3T MRSI data for automatic tissue characterization of the prostate

Teresa Laudadio[a]*, Anca R. Croitor Sava[b,c], Diana M. Sima[b,c], Alan J. Wright[d], Arend Heerschap[e], Nicola Mastronardi[a] and Sabine Van Huffel[b,c]

In this study non-negative matrix factorization (NMF) was hierarchically applied to simulated and *in vivo* three-dimensional 3 T MRSI data of the prostate to extract patterns for tumour and benign tissue and to visualize their spatial distribution. Our studies show that the hierarchical scheme provides more reliable tissue patterns than those obtained by performing only one NMF level. We compared the performance of three different NMF implementations in terms of pattern detection accuracy and efficiency when embedded into the same kind of hierarchical scheme. The simulation and *in vivo* results show that the three implementations perform similarly, although one of them is more robust and better pinpoints the most aggressive tumour voxel(s) in the dataset. Furthermore, they are able to detect tumour and benign tissue patterns even in spectra with lipid artefacts. Copyright © 2016 John Wiley & Sons, Ltd.

Keywords: MRSI; blind source separation; non-negative matrix factorization; prostate cancer; nosologic imaging

INTRODUCTION

Automatic and accurate non-invasive tissue characterization is an unmet need in the diagnosis and treatment-evaluation of tumours. The most reliable clinical tool to verify the presence of body tumours is, currently, biopsy, which carries a risk of morbidity or mortality. Furthermore, each biopsy samples only a single location in the tumour. Imaging technologies, such as MR modalities, are desirable as they allow a non-invasive diagnosis of the whole tumours. MRSI is a potential powerful tool, since it is able to provide metabolic information that could be used to localize and characterize tumour tissue non-invasively (1,2).

Currently, prostate MRSI data are often visualized as metabolite maps, in which the spatial distributions of the (relative) levels of metabolites in prostate cancer are displayed (3–5). Indeed, differences between normal prostate gland tissue, containing high levels of citrate (Citr), and prostate tumour tissue, which has higher levels of choline (Cho) containing compounds, have been observed (4). Quantification of these metabolite signals, however, may still be cumbersome if spectra have low signal to noise ratio (SNR) or broad overlapping peaks, or contain artefacts. Furthermore, quantification may be suboptimal due to differences among the spectra of different voxels (e.g. frequency shifts, line widths). Spectral pre-processing and visual quality control (QC) are often user dependent and time consuming, especially in the case of three-dimensional MRSI.

Alternatively, automatic segmentation and classification methods have been proposed for prostate MRSI data. These consist of supervised pattern recognition approaches that exploit prior knowledge in the form of models or a training set (6,7) in order to detect tumour voxels. However, such methods may be limited to MRSI data with particular acquisition parameters. Recently, a blind source separation (BSS) method

* *Correspondence to: Laudadio, Teresa, Consiglio Nazionale delle Ricerche, Istituto per le Applicazioni del Calcolo "M. Picone", Bari, Italy. E-mail: t.laudadio@ba.iac.cnr.it*

a *T. Laudadio, N. Mastronardi*
Istituto per le Applicazioni del Calcolo 'M. Picone' (IAC), Consiglio Nazionale delle Ricerche, Bari, Italy

b *A. R. Croitor Sava, D. M. Sima, S. Van Huffel*
Department of Electrical Engineering (ESAT), STADIUS Center for Dynamical Systems, Signal Processing and Data Analytics, KU Leuven, Leuven, Belgium

c *A. R. Croitor Sava, D. M. Sima, S. Van Huffel*
iMinds Medical Information Technologies, Leuven, Belgium

d *A. J. Wright*
Cancer Institute CRUK, University of Cambridge, Li Ka Shing Centre, Cambridge, UK

e *A. Heerschap*
Department of Radiology, Radboud University Nijmegen Medical Center, Nijmegen, Netherlands

Abbreviations used: *NMF, non-negative matrix factorization; SNR, signal to noise ratio; BSS, blind source separation; ICA, independent component analysis; Cho, choline; Spm, spermine; Cr, creatine; Citr, citrate; Lip, lipids; HNMF, hierarchical NMF; NNLS, non-negative least squares; SD, standard deviation; CorCoef, correlation coefficient; GS, Gleason score; QC, quality control; MEGA-PRESS, Mescher–Garwood point resolved spectroscopy; VOI, volume of interest.*

Copyright © 2016 John Wiley & Sons, Ltd.

known as non-negative matrix factorization (NMF) (8) has been applied to MRSI data of the brain (9–12) to extract tissue specific metabolic patterns without the need for any prior tissue model and without imposing strong statistical constraints. This is an advantage compared with other methods, such as independent component analysis (ICA) and principal component analysis, which assume mutual independence and uncorrelation among sources, respectively. Indeed, these constraints may not apply to *in vivo* MRSI data since spectra from different tissues can be correlated (10). Furthermore, NMF provides not only tissue specific metabolic patterns, but also their corresponding abundances, i.e. the contribution of extracted patterns to the spectra in each MRSI voxel. These allow a proper assessment of tissue mixtures, thereby representing an improvement over classical classification algorithms that label each voxel either as tumour or benign.

In the assessment of brain MRSI data by NMF, a hierarchical approach has been used consisting of progressively applying several NMF levels (9,10,12). Here, we propose an alternative recursive–hierarchical application of NMF (HNMF) to assess three-dimensional MRSI data of the prostate obtained at 3 T. We investigated and compared the performance of HNMF in accuracy of pattern detection with that of the non-hierarchical approach, which consists of only one NMF level. Moreover, since several NMF algorithms are available in the literature, we considered three different implementations: ALS-NMF (13), aHALS-NMF (14) and CONVEX-NMF (15). ALS-NMF is the most popular implementation in the BSS community; CONVEX-NMF and aHALS-NMF were successfully applied to brain MRSI data and were proven to perform better than other implementations (11,12). We embedded such implementations into HNMF, which formed the basis of an automatic tissue characterization method. Depending on the considered NMF algorithm, we denoted the method by ALS-HNMF, aHALS-HNMF and CONVEX-HNMF, respectively.

The three variants of the method were applied to simulated as well as to *in vivo* prostate MRSI data, and their performances were compared in terms of accuracy and efficiency.

EXPERIMENT

Simulation set-up

Two different simulated MRSI datasets were considered in order to assess the performance of the proposed tissue characterization approach: a dataset characterized only by tumour and benign tissue (Dataset 1), and a dataset including lipid artefacts (Dataset 2).

The simulated datasets were obtained as follows. Two MR spectral profiles, representing pure tumour and benign tissue (top left plots in Fig. 1), were considered as theoretical models and linearly combined in different percentages to simulate 10 MRSI datasets. The two spectral profiles were created based on the prior knowledge that proton MR spectra of the prostate contain only signals from Cho, spermine (Spm), creatine (Cr) and Citr, with tumour regions characterized by spectra with higher Cho and reduced Citr signals (3–5) (Appendix).

Each dataset consists of a grid of spectra computed as follows:

$$s = at + (1 - a)b, \qquad [1]$$

where t and b stand for the pure tumour and benign model spectra, respectively, and $a \in [0, 1]$ gives the proportion of tumour in each voxel.

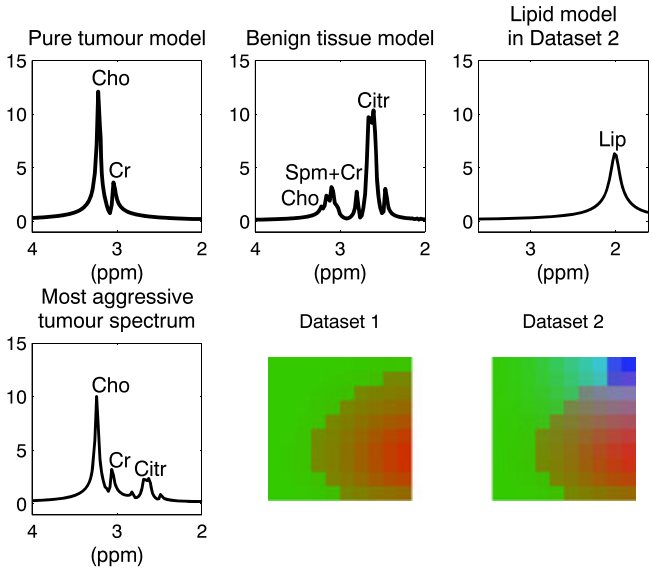

Figure 1. Top row (from left to right): prostate model magnitude spectra assumed for pure tumour, benign tissue and lipids. Bottom row: most aggressive tumour spectrum in Datasets 1 and 2; nosologic image for Dataset 1; nosologic image for Dataset 2. Voxel colours range from red (aggressive tumour) to green (benign tissue) to blue (lipids).

Furthermore, spectra were randomly frequency shifted by up to ±0.0396 ppm to simulate realistic MRSI datasets. The aforementioned values cover the typical shifts occurring in *in vivo* datasets such as those described in the next subsection.

Dataset 1 consists of a 10 × 10 grid of voxels mimicking a highly aggressive prostate tumour (bottom middle image in Fig. 1), where the contribution of the pure tumour model ranges from 20% to 80%. The spectrum with the highest contribution of the pure tumour model is displayed in Fig. 1, bottom left image.

Dataset 2 was obtained by adding a region containing lipid artefacts to Dataset 1 (blue region in the bottom right image of Fig. 1). The lipid signal (Lip – top right image in Fig. 1) was modelled as a broad Lorentzian peak (16) with line width comparable to that of the lipid signals observable in the available *in vivo* datasets.

Signals were perturbed by adding different levels of Gaussian noise with known standard deviation (SD). Each spectrum was normalized by dividing it by its l2-norm (17).

In vivo MRSI examinations

Three-dimensional 3 T MRSI data were acquired in six patients affected by prostate cancer with different Gleason scores (GSs) at the Radboud University Medical Centre (RUMC, Nijmegen, The Netherlands) on a Siemens (Erlangen, Germany) Magnetom Trio scanner as follows: an endorectal surface coil (MEDRAD, Bayer HealthCare, Whippany, NJ, USA) was combined with body array coils for signal reception; a Mescher–Garwood point resolved spectroscopy (MEGA-PRESS) pulse sequence was used with T_E = 145 ms, T_R = 750 ms, number of phase-encoding steps (x, y, z) = 12 and a vector size of 512 points at a receiver bandwidth of 1250 Hz (18,19). MEGA pulses (20) were applied for frequency-selective water and fat suppression, and spatial lipid saturation slabs were placed around the volume of interest (VOI). The MRSI field of view, matrix size and number of weighted acquisitions were adapted to the individual patient, resulting in a nominal voxel size

Copyright © 2016 John Wiley & Sons, Ltd.

NMR IN BIOMEDICINE

before apodization of either $5\times5\times5\,mm^3$ or $6\times6\times6\,mm^3$ in a total acquisition time of 9 min. The study was approved by the ethical committee. All patients subsequently underwent radical prostatectomy, and a prostate specimen was fixated with formalin and labelled by inking of the surface, followed by serially sectioning at 4 mm intervals perpendicular to the dorsal–rectal surface (21). The resulting slices were macroscopically photographed. A urologic pathologist outlined the location of the tumour on these histopathological images and graded each focus according to Reference (22). Patients were then staged following the 2002 TNM classification (23).

In this paper we used the histological photographs to illustrate the localization of the tumour foci, but a registration correcting for distortions was not performed. The MRSI voxels within the tumour or normal region, as outlined based on the histopathological images, were labelled by an expert spectroscopist as 'tumour' or 'normal', provided that these spectra were of sufficient quality (sufficient SNR, absence of lipid signals and absence of baseline distortions). The experts' criteria for defining acceptable SNR and unacceptable lipid and baseline distortions are reported in Reference (24). For each patient, the selected signals were fitted using a prototype software package (Metabolite Report, Siemens). Since Cho/Citr or (Cho + Cr)/Citr are often used as biomarkers to detect tumour tissue in prostate, among the tumour labelled voxels the voxel characterized by the spectrum with highest (Cho + Cr)/Citr was determined and assigned as the most aggressive tumour voxel (21). This spectrum was used in the *in vivo* studies to evaluate the accuracy of the tumour pattern provided by the method proposed in this paper.

THEORY AND METHOD

NMF

NMF is a BSS technique imposing non-negative constraints on the extracted sources and corresponding weights. Specifically, given a non-negative matrix $X \epsilon R^{mxn}$, and an integer k $(0 < k < \min(m, n))$ representing the number of sources to extract, two non-negative matrices, $W \epsilon R^{mxk}$ (source matrix) and $H \epsilon R^{kxn}$ (weight matrix), are estimated by minimizing the functional

$$f(W,H) = \frac{1}{2}\|X - WH\|_F^2 \qquad [2]$$

where the subscript F stands for the Frobenius norm (17). It is worth noticing that, given the non-convex nature of $f(W,H)$, its minimization may lead to the estimation of local minima and does not admit a unique solution. Several NMF algorithms have been proposed in order to deal with this problem (13). In this paper we consider the following ones:

1 ALS-NMF (13), available in MATLAB (MathWorks, Natick, Massachusetts, USA) and based on an alternating least squares scheme;
2 aHALS-NMF (14), an accelerated version of the hierarchical alternating least-squares scheme proposed in Reference (25);.
3 CONVEX-NMF (15), where the columns of W, i.e. the sources, are restricted to convex combinations of the columns of the data matrix X.

Starting values for aHALS-NMF and CONVEX-NMF, whenever applied, will be provided by ALS-NMF.

In the following, the above NMF implementations will be embedded into the recursive hierarchical scheme we propose in this paper, i.e. HNMF, and this will be included in an automatic tissue characterization method, which, depending on the considered NMF variant, will be respectively denoted by ALS-HNMF, aHALS-HNMF and CONVEX-HNMF.

Tissue characterization method based on HNMF

The input to NMF consists of a matrix where the pre-processed MRSI magnitude spectra are stacked as columns. NMF was first applied to each dataset by setting k, the number of tissues to detect, equal to 2. Nevertheless, preliminary results revealed this approach to be unreliable, and we therefore embedded NMF into the recursive–hierarchical scheme described later (see *Tissue characterization method*). The hierarchical scheme generates many tissue-representative spectral profiles from increasingly finer partitions of the MRSI grid.

The *in vivo* MR spectra were pre-processed by HLSVD-PRO (26) in order to remove water and lipid contributions. Furthermore, an automatic and fast QC algorithm (24) was applied to assess the quality of each spectrum in the VOI. Only spectra labelled as of sufficient quality, here denoted as QC spectra, were considered for further analysis.

Tissue characterization method

Step 1. HNMF.
The MRSI dataset is arranged into a matrix X, containing spectra as columns, and NMF is applied to X by setting $k = 2$. Two source signals and their corresponding weights are obtained.
The columns in the source matrix W are normalized by dividing each column by its l2-norm, and the rows in the weight matrix H are scaled accordingly. The given MRSI voxels are divided into two new datasets by assigning each voxel to the source signal characterized by the maximum weight in that voxel.
The procedure is recursively repeated after building new X matrices from spectra pertaining to each of the subsets obtained above.

In this study, four NMF levels, corresponding to increasingly finer partitions of the initial MRSI data, were applied and a cumulative number of 30 source signals were obtained. Two sources, representing tumour and benign tissues, were automatically selected as tissue patterns based on the prior knowledge that Cho/Citr should be high for tumour and low for benign tissue. Moreover, the source with the most predominant peak in the region (1.7 ppm–2.3 ppm) was selected as the lipid pattern. The selection procedure used integration to determine peak amplitudes.

Step 2. Non-negative least squares (NNLS) (27) is applied to X by simultaneously using the final patterns of Step 1 as regressors. Coefficient vectors are obtained (one for each pattern), which can be plotted for their MRSI voxel's positions to give tissue maps. These maps are encoded as colour channels in an RGB image, thereby providing a simultaneous visualization of the considered tissues as well as of their mixture. Such an image is called an unsupervised nosologic image (9), as different tissue types are denoted by different colours: red for tumour, green for benign tissue, blue for lipids, and their possible mixture for mixed tissue.

A pseudocode along with some MATLAB codes is available at http://users.ba.cnr.it/iac/irmanm21/Welcome_Teresa_files/HNMF_codes.pdf.

Copyright © 2016 John Wiley & Sons, Ltd.

Performance measures

The performance of ALS-HNMF, aHALS-HNMF and CONVEX-HNMF is assessed in terms of detection accuracy and efficiency. Specifically, the pattern detection accuracy is estimated by computing the correlation coefficient (CorCoef) between the final tissue patterns provided by each variant of the method and the assumed spectral tissue models. The spatial detection accuracy is obtained by computing the CorCoef between the coefficients in the tissue maps provided by NNLS and those in the simulated maps.

Finally, in the *in vivo* studies, Cho/Citr maps are estimated by peak integration and are compared with the tumour maps provided by the NMF-based methods.

RESULTS

Simulation studies

One ALS-NMF level with $k = 2$, and Step 1 of ALS-HNMF, aHALS-HNMF and CONVEX-HNMF, were applied to Dataset 1 with a medium noise level (SD = 0.04). The detected tumour (red) and benign (green) tissue patterns are superimposed on the theoretical models (black) in Fig. 2.

The CorCoef values between the detected patterns and the theoretical models as well as the spatial CorCoef values were estimated (Table 1). Such values show that the hierarchical approach significantly outperforms the single-level ALS-NMF.

The results obtained in Step 2 of ALS-HNMF are displayed in Fig. 3. The pathological region is visualized in red in the nosologic image and it corresponds well to the original simulated one (bottom middle image of Fig. 1).

ALS-HNMF, aHALS-HNMF and CONVEX-HNMF were applied to Dataset 1 and Dataset 2 over 300 simulation runs for different noise levels. The CorCoef means and corresponding SDs (see Figs. 4 and 5) reveal excellent performance of the three HNMF implementations for Dataset 1. Good values are obtained for Dataset 2 except for the largest noise level, SD = 0.1. Furthermore, although the three methods perform similarly,

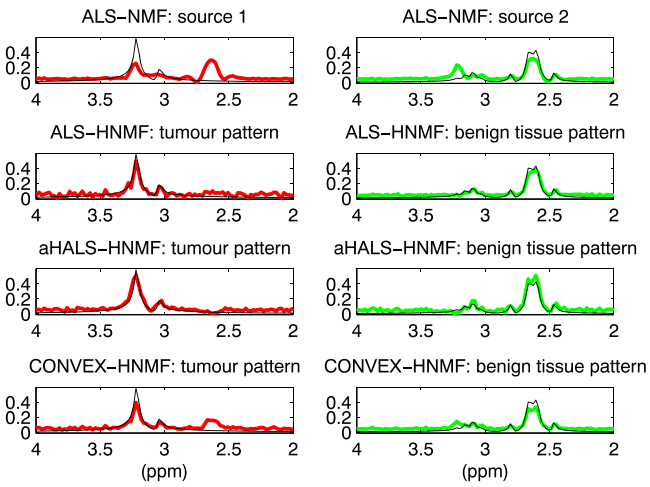

Figure 2. From top to bottom: sources obtained by applying to Dataset 1 one level of ALS-NMF with $k = 2$ (first row plots), final tumour (red) and benign (green) tissue patterns provided by ALS-HNMF (second row), aHALS-HNMF (third row) and CONVEX-HNMF (fourth row), superimposed on the theoretical tissue models (black).

Table 1. Simulation results obtained by applying one ALS-NMF level with $k = 2$, ALS-HNMF, aHALS-HNMF and CONVEX-HNMF to dataset 1 for one simulation run and SD = 0.04. CorCoef between detected tumour patterns and tumour model (a), benign patterns and benign model (b), NNLS tumour maps and simulated tumour map (c) and NNLS benign maps and simulated benign tissue map (d)

Methods	(a)	(b)	(c)	(d)
ALS-NMF ($k = 2$)	0.5054	0.8889	0.3005	0.6940
ALS-HNMF	0.9074	0.9734	0.9581	0.9829
aHALS-HNMF	0.9486	0.9584	0.9623	0.9852
CONVEX-HNMF	0.8736	0.9739	0.9615	0.9775

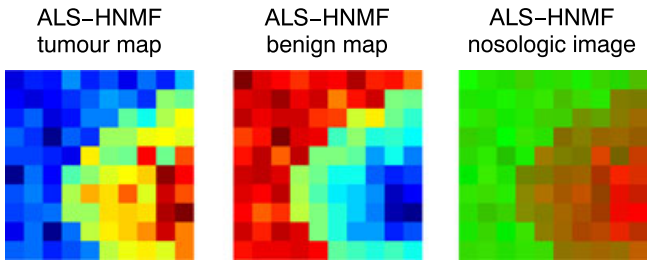

Figure 3. Tissue maps and nosologic image obtained by ALS-HNMF for Dataset 1 in one simulation run with SD = 0.04. In the nosologic image the pathological and benign regions are visualized with the red and green intensities, respectively.

CONVEX-HNMF is more robust as it generally exhibits the lowest SDs.

All the implementations are efficient as they require about 1 s of computation time to process each dataset.

In vivo studies

Tests were also carried out on the *in vivo* datasets described earlier to validate the results obtained by the simulation studies.

The CorCoef values between the final patterns and the corresponding theoretical models, between the tumour pattern and the most aggressive tumour spectrum selected by the experts and between the tumour map and the Cho/Citr map for all the considered patients are reported in Table 2 (Columns 5–8). Observe that CONVEX-HNMF always provides the detection results that best correlate with the most aggressive tumour spectrum and with the Cho/Citr map (Columns 7 and 8, respectively). For Patients 3 and 6, ALS-HNMF performs best in terms of tumour pattern detection compared with the 'pure' tumour model. It is worth observing that for Patient 2 the extracted tumour patterns are weakly correlated with the most aggressive tumour spectrum. A visual inspection of this spectrum revealed that it contains a significant Citr peak, while the three implementations of HNMF detect patterns without or very low Citr contribution. The reason for this difference is that expert labelling only involved some of the QC spectra, and in this case did not consider spectra with a low contribution of Citr.

Also in the case of Patient 6, ALS-HNMF and aHALS-HNMF provide a tumour pattern that is weakly correlated with the most aggressive tumour spectrum. CONVEX-HNMF finds a tumour pattern better correlated with the aforementioned spectrum,

Copyright © 2016 John Wiley & Sons, Ltd.

NMR IN BIOMEDICINE

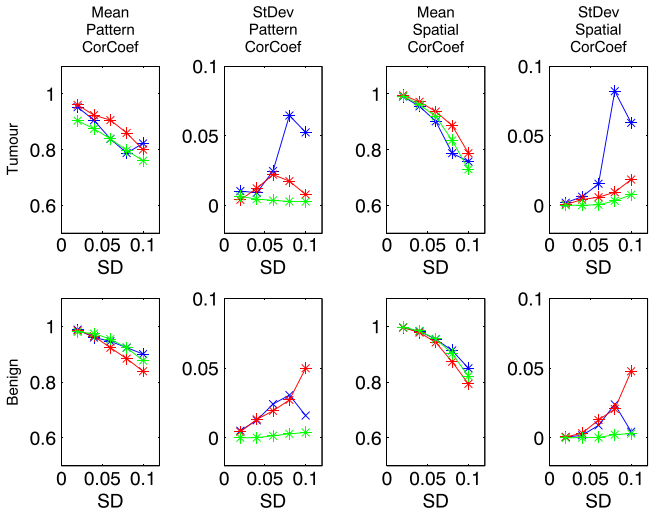

Figure 4. Dataset 1. Means (plots in Columns 1 and 3) and corresponding SDs (plots in Columns 2 and 4) of the CorCoef values between the final tissue patterns and the corresponding theoretical models (Columns 1 and 2), and of the spatial CorCoef values (Columns 3 and 4) obtained with ALS-HNMF (blue), aHALS-HNMF (red) and CONVEX-HNMF (green) over 300 runs and for different SDs.

although this pattern is the least correlated with the theoretical tumour model.

The detection results obtained by CONVEX-HNMF for Patient 1 are displayed in Fig. 6 as an example of HNMF analysis. The QC algorithm was applied to the spectra inside the VOI, revealing that spectra of sufficient quality are mostly located in Slices 5–10. The percentage of voxels discarded by the QC algorithm was 13% for the illustrated slice, 17% over slices 5–10, and 38% over all slices. CONVEX-HNMF was applied to the QC spectra and provided tumour (red curve in Fig. 6) and benign (green curve) tissue patterns highly correlated with the theoretical

Table 2. *In vivo* results. Column 5, CorCoef between the tumour pattern (TP) and the theoretical tumour model (TM); column 6, CorCoef between the benign tissue pattern (BP) and the theoretical benign model (BM); column 7, CorCoef between the tumour pattern and the most aggressive tumour spectrum (MAT) provided by expert labelling; column 8, mean CorCoef value over all slices between the tumour map (Tmap) and the Cho/citr map

Patients	Age	GS	Methods (HNMF)	TP versus TM	BP versus BM	TP versus MAT	Tmap versus Cho/Citr
1	61	4+3	ALS	0.8668	0.9458	0.8259	0.9673
			aHALS	0.8748	0.8162	0.8400	0.9748
			CONVEX	0.8728	0.9425	0.8510	0.9764
2	66	4+3	ALS	0.9128	0.9327	0.5900	0.9404
			aHALS	0.9060	0.9557	0.4888	0.9264
			CONVEX	0.9014	0.9300	0.6624	0.9659
3	67	4+3	ALS	0.8722	0.9193	0.7929	0.9429
		+5	aHALS	0.8193	0.9233	0.6702	0.9033
			CONVEX	0.7568	0.9299	0.8540	0.9629
4	64	3+4,	ALS	0.8851	0.9246	0.7811	0.9108
		4+3	aHALS	0.8541	0.9026	0.7060	0.8891
			CONVEX	0.8897	0.9290	0.8686	0.9655
5	70	4+3,	ALS	0.8438	0.9584	0.5863	0.8687
		3+3	aHALS	0.8164	0.9587	0.5648	0.8404
			CONVEX	0.8095	0.9647	0.7865	0.9225
6	66	4+3	ALS	0.7287	0.9599	0.5762	0.8540
		+5	aHALS	0.6104	0.9654	0.3448	0.8085
			CONVEX	0.4351	0.9578	0.9096	0.9349

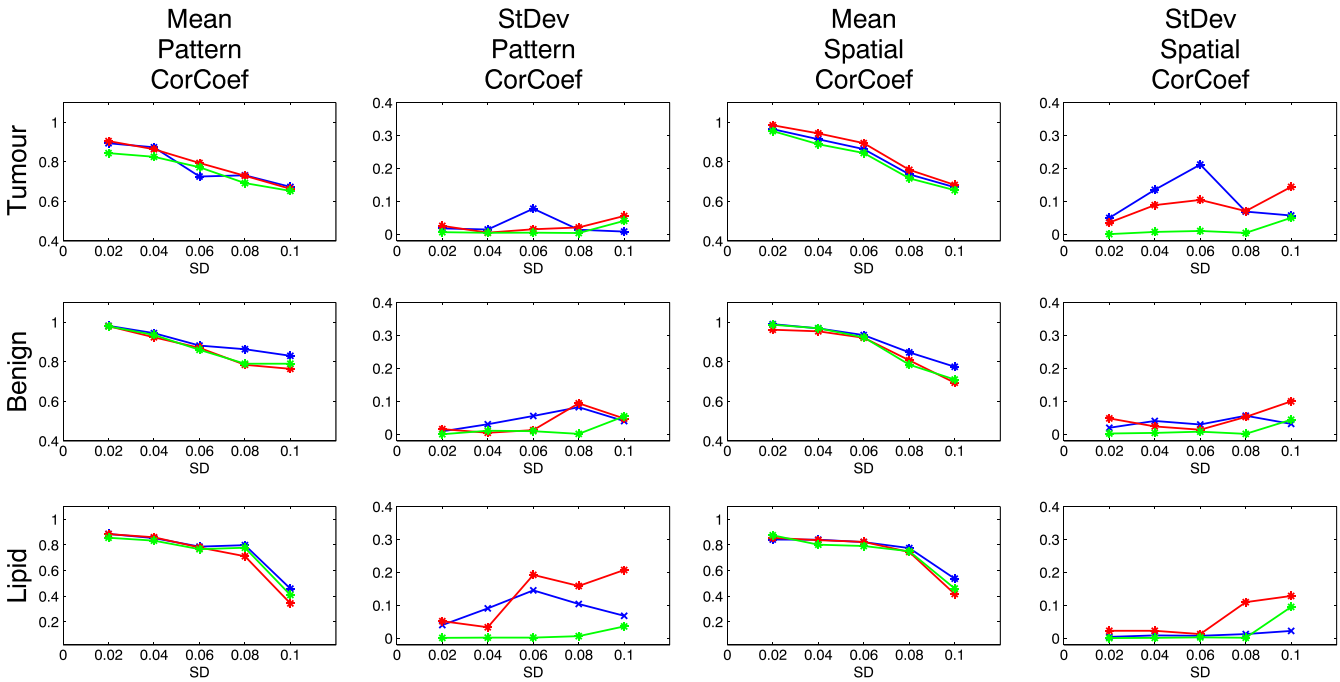

Figure 5. Dataset 2. Means (plots in Columns 1 and 3) and corresponding SDs (plots in Columns 2 and 4) of the CorCoef values between the final tissue patterns and the corresponding theoretical models (Columns 1 and 2), and of the spatial CorCoef values (Columns 3 and 4) obtained with ALS-HNMF (blue), aHALS-HNMF (red) and CONVEX-HNMF (green) over 300 runs and for different SDs.

Copyright © 2016 John Wiley & Sons, Ltd.

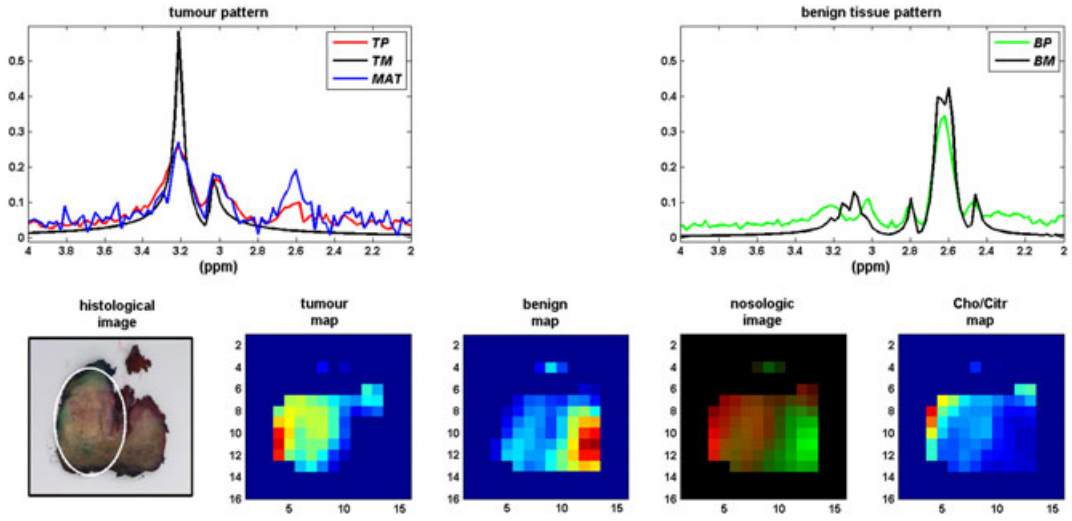

Figure 6. Patient 1. Top plots: tumour (red) and benign (green) tissue patterns obtained by CONVEX-HNMF versus theoretical models (black) and versus the most aggressive tumour spectrum (blue spectrum in the left-hand plot). Bottom images, from left to right: histopathological image where the tumour region is indicated on a resected slice of the prostate approximately corresponding to the axial image; tissue maps obtained by Step 2; nosologic image; Cho/Citr map. In the maps only the good quality voxels are visualized. In the nosologic image the pathological area is displayed in red, the benign tissue in green and mixed tissue in a mixture of the aforementioned colours. In the Cho/Citr map, the higher the intensity of colour the larger the Cho/Citr value in the considered voxel.

models (black curves) as well as with the most aggressive tumour spectrum (blue curve in the top left plot). Moreover, in agreement with histopathology, the nosologic image correctly visualizes the pathological region, and the tumour map corresponds very well to the Cho/Citr map, as also confirmed by the CorCoef value in Table 2 (Column 8).

DISCUSSION

In this paper NMF was hierarchically applied to simulated as well as to *in vivo* prostate MRSI data in order to extract characteristic patterns for prostate tissues and to visualize their spatial distributions by means of unsupervised nosologic images. These colour images summarize the spectral information from the MRSI dataset measured in a patient. Although they do not represent tumour probability maps and they cannot be compared across patients, these images are an efficient way to visualize the spatial distribution of relevant tissue patterns in the dataset. They should only be interpreted together with the corresponding extracted tissue patterns.

NMF algorithms have already been applied successfully to brain MRSI data, but, to our knowledge, this study represents the first example of application of NMF to prostate MRSI data.

In the simulation studies, the MRSI spectra were generated using only two models for 'pure' tumour spectra and benign spectra (1). This is a simplified approach to real prostate MRSI data, which may also present different spectral features, both in the benign tissue (e.g. differences between peripheral and central gland, partial volume from the seminal vesicle areas) and in the tumour (e.g. differences between tumour grades).

We first observed that, for all the considered NMF implementations, the hierarchical scheme provides tissue patterns of higher quality than those from one NMF level with k equal to the number of tissue patterns to detect. Applying one NMF level by increasing the value of k would also be possible, but an automatic selection of the optimal k ensuring the presence of both the tumour and benign tissue patterns among the obtained sources is needed. This represents a model order selection problem and is beyond the scope of the present paper.

The second objective of our study was to compare the performance of ALS-HNMF, aHALS-HNMF and CONVEX-HNMF in detection accuracy and efficiency.

The simulation results showed that the three considered variants of the method perform similarly. Nevertheless, CONVEX-HNMF is recommended since it is more robust and always provides patterns that are linear combinations of the existing spectra in the MRSI dataset. Indeed, it better pinpoints the most aggressive tumour voxel(s) because the tumour pattern is very similar to some of the spectra in the dataset. Regarding aHALS-HNMF, the simulation studies showed its tendency to find sources that are less correlated with each other, e.g. a source that was flat or had a dip where the second source had a peak. Thus, aHALS-HNMF would be more appropriate if the aim is to find the underlying uncorrelated sources in the data, but less appropriate if the goal is to detect and visualize the most aggressive part of the MRSI dataset. Finally, ALS-HNMF sometimes shows a behaviour similar to that of CONVEX-HNMF, sometimes to that of aHALS-HNMF, without a clear trend.

Regarding the tumour region detection, the spatial CorCoef values revealed that the three variants perform similarly. This is not perfectly in agreement with the results obtained for the tumour pattern detection, where CONVEX-HNMF showed a slightly worse performance. This is due to the shape of the most aggressive tumour spectra, which often contain a Citr contribution, while no Citr multiplet is present in our 'pure' tumour model.

Several advantages characterize the method proposed in this paper when compared with either the classical approach based on the estimation of metabolite maps or other NMF-based algorithms. Indeed, as shown in the *in vivo* studies, our method automatically provides tumour maps that are highly correlated with the Cho/Citr maps, but they also correlate to the underlying

Copyright © 2016 John Wiley & Sons, Ltd.

NMR IN BIOMEDICINE

tissue pattern. It thus gives a direct and simultaneous visualization of the tissue pattern distributions without the need for any thresholding procedure, and it also accommodates the visualization of tissue mixtures.

Moreover, the construction of metabolite maps may be difficult if signals contain broad overlapping peaks or have artefacts or differences in frequency shifts and line widths. In this paper, the first two limitations were overcome by applying two automatic pre-processing algorithms, i.e. HLSVD-PRO and the QC algorithm. The former was used to filter out the water and lipid contributions; the latter was applied to select spectra of sufficient quality.

The results of the QC algorithm showed that acceptable spectra are mostly located in the middle slices. Furthermore, the simulation studies revealed that possible lipid artefacts can be detected as separate sources without significantly affecting the accuracy of the tumour and benign tissue patterns. Here, it is worth highlighting that slightly worse results were obtained for the tumour pattern when processing Dataset 2. These are due to the pattern selection criterion adopted in Step 1 of the method. Indeed, sometimes the source signal exhibiting the highest Cho/Citr contains also a lipid peak, thereby affecting the performance of the method in terms of CorCoef values. Such a drawback can be overcome by properly modifying the above criterion to take into account not only Cho and Citr, but also lipids.

Obviously, when the water signal is not filtered out, the predominant water peak will strongly affect the HNMF source extraction. Therefore, water removal is recommended before applying HNMF.

Concerning possible differences among spectra, frequency shifts were included in the simulation studies. In general, the approximate linear model assumed by HNMF is not satisfied when spectra within an MRSI dataset have significantly different frequency shifts or line widths, which might arise from an inhomogeneous magnetic field. Nevertheless, *a priori* correction is non-trivial and has not been applied, since Step 1 of the method provides a cumulative number of 30 source signals: some of them are possible candidates for tumour tissue, some for benign tissue and the remaining ones for mixed tissue, but all of them capture the most representative frequency shifts and line widths occurring in the whole dataset. The NNLS step (Step 2 of the method) would lead to nosologic images where the spectra affected by too large distortions (e.g. broad line widths) are not well modelled by the final sources. Such modelling errors could be visualized as an error map as proposed in Reference (9).

Regarding the comparison with other NMF-based algorithms, in the first section we refer to several NMF algorithms developed for processing brain MRSI data, i.e. References (9–12). In particular, the main purpose of the methods proposed in References 10 and 11 consists in the separation of tumour versus non-tumour tissue, which does not take into account the fact that the detection of other characteristic pure tissues is crucial for therapy planning. In contrast, as reported above, HNMF can be applied to detect more than two pure tissue types (i.e. tumour, benign and lipid tissue) along with their mixtures. An alternative method is described in References (9) and (12), which could be properly modified and applied to prostate MRSI data. Nevertheless, it assumes that the first NMF level in the hierarchical scheme is able to extract an accurate healthy tissue pattern and the second NMF level is only aimed at differentiating abnormal tissue patterns. In the case of prostate MRSI data, our studies show that the first NMF level does not provide a reliable benign tissue pattern. Furthermore, in References (9) and (12) a thresholding procedure is included in the second NMF level, which makes the algorithm slightly more complex and computationally more expensive than our method.

Finally, HNMF would be expected to work similarly for data acquired with different MRSI sequences. These sequences would have different underlying spectral tissue patterns depending on the repetition and echo times.

Despite the attractive properties listed above, an open problem is represented by the choice of the NMF levels to include in Step 1 of the method. Our studies show that four NMF levels allow the extraction of high quality tissue patterns. Nevertheless, an automatic procedure would be desirable rather than the heuristic one adopted in this study, and this will be the subject of future research.

CONCLUSIONS

We propose an automatic and fast tissue characterization method, based on a hierarchical application of NMF to prostate MRSI data. The method is able to detect tissue-representative patterns and to visualize their spatial distributions without requiring prior tissue models or strong statistical constraints. Moreover, some data pre-processing steps may not be needed because the method appears to provide good results even in the presence of low SNR signals, lipid artefacts and variations in chemical shift among voxels.

Since several NMF algorithms are available in the literature, we compared the performance of three different NMF implementations in terms of pattern detection accuracy and efficiency when embedded in the proposed method. Our studies show that CONVEX-HNMF is the most robust variant and it better pinpoints the most aggressive tumour voxel(s) in the dataset.

Acknowledgements

T. Laudadio is partly supported by PRIN 2012 N. 2012MTE38N and Progetto Premiale MIUR 2012 (MATHTECH). A. R. Croitor Sava, D. Sima and S. Van Huffel are supported by FWO project G.0869.12 N (Tumor Imaging), iMinds Medical IT, ERC Advanced Grant BIOTENSORS (No 339804) and EU MC ITN TRANSACT 2012 (No 316679).

REFERENCES

1. Hoeks CMA, Barentsz JO, Hambrock T, Yakar D, Somford DM, Heijmink SWTPJ, Scheenen TWJ, Vos PC, Huisman H, Van Oort IM, Witjes JA, Heerschap A, Futterer J. Prostate cancer: multiparametric MR imaging for detection, localization, and staging. Radiology 2011; 261(1): 46–66.
2. Öz G, Alger JR, Barker PB, Bartha R, Bizzi A, Boesch C, Bolan PJ, Brindle KM, Cudalbu C, Dinçer A, Dydak U, Emir UE, Frahm J, González RG, Gruber S, Gruetter R, Gupta RK, Heerschap A, Henning A, Hetherington HP, Howe FA, Hüppi PS, Hurd RE, Kantarci K, Klomp DW, Kreis R, Kruiskamp MJ, Leach MO, Lin AP, Luijten PR, Marjańska M, Maudsley AA, Meyerhoff DJ, Mountford CE, Nelson SJ, Pamir MN, Pan JW, Peet AC, Poptani H, Posse S, Pouwels PJ, Ratai EM, Ross BD, Scheenen TW, Schuster C, Smith IC, Soher BJ, Tkáč I, Vigneron DB, Kauppinen RA, MRS Consensus Group. Clinical proton MR spectroscopy in central nervous system disorders. Radiology 2014; 270(3): 658–679.
3. Kobus T, Wright AJ, Scheenen TW, Heerschap A. Mapping of prostate cancer by ^{1}H MRSI. NMR Biomed. 2014; 27(1): 39–52.

 Copyright © 2016 John Wiley & Sons, Ltd.

4. Selnaes KM, Gribbestad IS, Bertilsson H, Wright A, Angelsen A, Heerschap A, Tessem MB. Spatially matched *in vivo* and *ex vivo* MR metabolic profiles of prostate cancer – investigation of a correlation with Gleason score. NMR Biomed. 2013; 26(5): 600–606.
5. Kurhanewicz J, Vigneron DB. Advances in MR spectroscopy of the prostate. Magn. Reson. Imaging Clin. N. Am. 2008; 16(4): 697–710.
6. Laudadio T, Pels P, De Lathauwer L, Van Hecke P, Van Huffel S. Tissue segmentation and classification of MRSI data using canonical correlation analysis. Magn. Reson. Med. 2005; 54: 1519–1529.
7. Kelm BM, Menze BH, Zechmann CM, Baudendistel KT, Hamprecht FA. Automated estimation of tumor probability in prostate magnetic resonance spectroscopic imaging: pattern recognition vs quantification. Magn. Reson. Med. 2007; 57(1): 150–159.
8. Lee DD, Seung HS. Learning the parts of objects by non-negative matrix factorization. Nature 1999; 401: 788–791.
9. Li Y, Sima DM, Van Cauter S, Croitor Sava AR, Himmelreich U, Pi Y, Liu Y, Van Huffel S. Unsupervised nosologic imaging for glioma diagnosis. IEEE Trans. Biomed. Eng. 2013; 60(6): 1760–1763.
10. Sajda P, Du S, Brown TR, Stoyanova R, Shungu DC, Mao X, Parra LC. Nonnegative matrix factorization for rapid recovery of constituent spectra in magnetic resonance chemical shift imaging of the brain. IEEE Trans. Med. Imaging 2004; 23: 1453–1465.
11. Ortega-Martorell S, Lisboa PJ, Vellido A, Simões RV, Pumarola M, Julià-Sapé M, Arús C. Convex non-negative matrix factorization for brain tumor delimitation from MRSI data. PLoS One 2012; 7(10): e4.
12. Li Y, Sima DM, Van Cauter S, Croitor Sava AR, Himmelreich U, Pi Y, Van Huffel S. Hierarchical non-negative matrix factorization (hNMF): a tissue pattern differentiation method for glioblastoma multiforme diagnosis using MRSI. NMR Biomed. 2013; 26(3): 307–319.
13. Berry MW, Browne M, Langville AN, Pauca VP, Plemmons RJ. Algorithms and applications for approximate nonnegative matrix factorization. Comput. Stat. Data Anal. 2007; 52: 155–173.
14. Gillis N, Glineur F. Accelerated multiplicative updates and hierarchical ALS algorithms for nonnegative matrix factorization. Neural Comput. 2012; 24: 1085–1105.
15. Ding C, Li T, Jordan M. Convex and semi-nonnegative matrix factorizations. IEEE Trans. Pattern Anal. Machine Intell. 2010; 32: 45–55.
16. Wright AJ, Heerschap A. Simple baseline correction for ^{1}H MRSI data of the prostate. Magn. Reson. Med. 2012; 68(6): 1724–1730.
17. Golub GH, Van Loan CF. *Matrix Computations*, 4th edn. Johns Hopkins University Press: Baltimore, MD, 2013.
18. Scheenen TW, Klomp DW, Röll SA, Fütterer JJ, Barentsz JO, Heerschap A. Fast acquisition-weighted three-dimensional proton MR spectroscopic imaging of the human prostate. Magn. Reson. Med. 2004; 52(1): 80–88.
19. Verma S, Rajesh A, Futterer JJ, Turkbey B, Scheenen TW, Pang Y, Choyke PL, Kurhanewicz J. Prostate MRI and 3D MR spectroscopy: how we do it. Am. J. Roentgenol. 2010; 194(6): 1414–1426.
20. Mescher M, Tannus A, Johnson MO, Garwood M. Solvent suppression using selective echo dephasing. J. Magn. Reson. A 1996; 123(2): 226–229.
21. Kobus T, Hambrock T, de Kaa Hulsbergen-Van CA, Wright AJ, Barentsz JO, Heerschap A, Scheenen TW. In vivo assessment of prostate cancer aggressiveness using magnetic resonance spectroscopic imaging at 3 T with an endorectal coil. Eur. Urol. 2011; 60(5): 1074–1080.
22. Epstein JI, Allsbrook WC, Jr, Amin MB, Egevad LL, ISUP Grading Committee. The 2005 International Society of Urological Pathology (ISUP) consensus conference on Gleason grading of prostatic carcinoma. Am. J. Surg. Pathol. 2005; 29: 1228–1242.
23. Greene FL, Page DL, Flemming ID, Fritz A, Balch CM, Haller DG, Morrow M. *AJCC Cancer Staging Manual*, 6th edn. Springer: New York, 2002.
24. Wright AJ, Kobus T, Selnæs KM, Gribbestad IS, Weiland E, Scheenen TWJ, Heerschap A. Quality control of prostate ^{1}H MRSI data. NMR Biomed. 2013; 26(2): 193–203.
25. Cichocki A, Zdunek R, Amari S. Hierarchical ALS algorithms for nonnegative matrix and 3D tensor factorization. Lect. Notes Comput. Sci. 2007; 4666: 169–176.
26. Laudadio T, Mastronardi N, Vanhamme L, Van Hecke P, Van Huffel S. Improved Lanczos algorithms for blackbox MRS data quantitation. J. Magn. Reson. 2002; 157: 292–297.
27. Lawson CL, Hanson RJ. *Solving Least Squares Problems*. Prentice Hall: Englewood Cliffs, NJ, USA, 1974 ch. 23, p., pp. 161.
28. Kobus T, Wright AJ, Van Asten JJ, Heerschap A, Scheenen TW. In vivo ^{1}H MR spectroscopic imaging of aggressive prostate cancer: can we detect lactate? Magn. Reson. Med. 2014; 71(1): 26–34.
29. Provencher SW. Estimation of metabolite concentrations from localized *in vivo* proton NMR spectra. Magn. Reson. Med. 1993; 30 (6): 672–679.

APPENDIX

Generation of Prostate mrs Profiles

The benign and pure tumour spectral profiles were obtained by quantification of three-dimensional 3T MRSI metabolite signals measured in patients affected by prostate cancer. Voxels within tumour or benign tissue were selected as part of a previous study (21) with a further selection for those that passed the QC algorithm. Basis spectra for Cho, Cr, Spm and Citr were generated with NMRSIM (Bruker, Karlsruhe, Germany) using a simulated MRSI sequence (28) with the same timings as the acquisition sequence (18). These basis spectra were then used to quantify the set of spectra using LCModel (29). The relative concentrations of the different metabolites for all the benign spectra were used to calculate the relative mean metabolite concentrations present in benign tissue. The benign tissue model spectrum is a combination of the four model metabolite spectra at these relative mean amounts. Concerning the pure tumour model, it was assumed that the spectra would consist of only Cho and Cr signals (3). ICA was performed on the full set of spectra to provide two components, one of which consisted of only two clear peak-like features corresponding to the chemical shifts of Cho and Cr. The relative amplitudes of these two 'peaks' were used to simulate the pure tumour model from a sum of the Cho and Cr simulated spectra.

Copyright © 2016 John Wiley & Sons, Ltd.